Niklaus RUTTIMANN[1]
Sebastian BUHL[2]
Konrad WEGENER[1]

SIMULATION OF SINGLE GRAIN CUTTING USING SPH METHOD

So-called Engineered Grinding Tools (EGT) have been developed in order to satisfy the industry's demand for more efficient and cost-effective grinding tools, which differ from classic grinding tools by placing and brazing single abrasive grains in a predefined pattern onto the grinding tool body. Single grain cutting simulations form an important part towards an advanced understanding of the engineered grinding process. Cutting simulations with FE Methods encounter problems arising from large deformation and material separation. These can be overcome using meshless methods. In this work, a Smooth Particle Hydrodynamics (SPH) Method is used to model the single diamond grain cutting, which can be used as the basis process for physical simulation of the grinding process. As results the influence of the grain geometry, grain orientation and grain placement on the cutting forces, the burr generation and the chip removal rate are presented. It is shown that the cutting forces for a given grain geometry as well as the burr generation are heavily influenced by the orientation of the minor and the main cutting faces. Also cutting in material being work hardened by preceding grains, is simulated in order to be able to synthesize the grinding process from single grain cutting.

1. INTRODUCTION

EGT are monolayer grinding tools, whose abrasive grains, mostly diamond and cubic boron nitride, are arranged in a predefined pattern on the grinding tool body [21] either by brazing [22],[23] or by electroplating [2]. The advantages of EGTs are a direct result of the predefined abrasive grain pattern. The grain pattern can be optimised in terms of chip space, material removal rate, coolant flow or achieved surface roughness [3,5,6,21,26,27]. The number of active grains of an EGT is lower than that of a conventional grinding tool, for this reason the load per grain is increased. Furthermore the shape and the orientation of the grain play in this case a more important role in the grinding process. A meaningful test to characterise such influences is the single grain cutting test. The simulation of this experiment is the key to a better understanding of the grinding process. In literature the

_____

[1] IWF - Institute of Machine Tools and Manufacturing, ETH Zuerich
[2] Empa - Swiss Federal Laboratories for Materials Science and Technology

points of interest are the chip formation mechanism [4],[18], the cutting forces [18] as well as the effect of the grain shape [15].

The grinding process with EGTs can be viewed as a collection of single grain cutting processes, interacting with other grains, the grinding tool, the machine tool and the work piece. The simulation of such a model is hampered by several problems. One problem is the huge span of length scales; the cutting depth is typically between 0.1 and 20 μm. On the other hand, the diamond grains have sizes from 200 to 1000 μm. The grinding tools have sizes in the mm to cm range. A simulation encompassing a complete grinding tool with a sufficiently fine discretisation to capture the necessary details around the cutting edge is therefore computationally too large for current computers. Tool simulations rely on analytical or empirical predictions for single grain forces [8].

The process on the single grain level can be separated into different parts; a rubbing phase, where the effects of friction, heat and elastic deformation of the workpiece are in focus, a ploughing phase, where material is deformed plastically but not removed as chip, and a cutting phase, where material is removed as chip, analogous to metal cutting with negative rake angles.

A detailed study of the material removal process necessitates the separation of the single grain from the overall grinding process to keep computational cost manageable. The state of the art tools to simulate metal cutting processes are Finite Element Methods (FEM, FE-methods). An overview over microscale single grain modelling and simulation can be found in [8] and newer works in [19],[20]. The majority of the publications use 2D FE-models [8],[17],[20] to modell the cutting phase and simulate forces and chip morphology. 3D FE-models are mostly used for the rubbing and ploughing phases [19]. This is due to the computational cost associated with simulating three-dimensional cutting processes using FEM.

The handling of large deformations and material separation poses a problem to classical FEM, which has to be circumvented using additional algorithms like Arbitrary Lagrange Euler (ALE) or adaptive mesh refinement algorithms, which are computationally expensive. Possible solutions are meshless or meshfree methods, which do not need a mesh to discretise a body and therefore have a metric that is attached to one single material element.

The Smoothed Particle Hydrodynamics (SPH) method used in this paper is the first meshless method and was developed by [14],[16] in 1977. The method was first used for metal cutting simulations in 1996 [10]. With the implementation of SPH in the commercial FE-Software LS-DYNA [9] the method became available to a wider audience. Since 2006, several works concerning the usage of SPH in metal cutting have been published [7],[12],[24], showing the utility of the method.

The goal of this work is to show the utility of simulating microcutting processes using SPH, analyse the influence of grain geometry, grain orientation and grain placement on the resulting cutting forces, the burr generation and the chip removal rates. The material presented here is part of the ongoing research efforts at IWF and EMPA to develop more efficient EGTs.

2. SMOOTH PARTICLE HYDRODYNAMICS

The basic approach of the SPH Method is to discretise a body with a cloud of points instead of an ordered mesh grid as in the case of FE-Methods. The field variables are represented by an integral expression over a finite domain Ω:

$$f(x) = \int_{\Omega} f(x')W(x-x',h)dx' \tag{1}$$

x is the coordinate of the node of interest, x' is the coordinate of an arbitrary point in the domain, W(x-x',h) is a weight or smoothing function and h is the smoothing length that defines the size of the domain that is used to approximate f(x). Eq. 1 can be approximated by a summation expression:

$$f(x) \cong \sum_{j=1}^{N} \Delta V_j f(x_j) W(x-x_j,h)$$

$$f(x) \cong \sum_{j=1}^{N} \frac{m_j}{\rho_j} f(x_j) W(x-x_j,h) \tag{2}$$

with ΔV_j the represented volume, m_j the mass and ρ_j the density. This step transforms the continuous integral in Eq. 1 into a discrete expression that only uses a selection of points at the coordinates x_j. As the SPH method uses a cloud of points x_i to represent a body, we approximate the field function at those nodes x_i according to:

$$f(x_i) \cong \sum_{j=1}^{N} \frac{m_j}{\rho_j} f(x_j) W(x_i - x_j,h) \tag{3}$$

Eq. 3 shows that a field at any given coordinate can be approximated as the weighted average of nodal values in a distance shorter than the smoothing length, as shown in Fig. 1. These nodes are called neighbour- or support nodes and the domain containing these nodes is the support or smoothing domain.
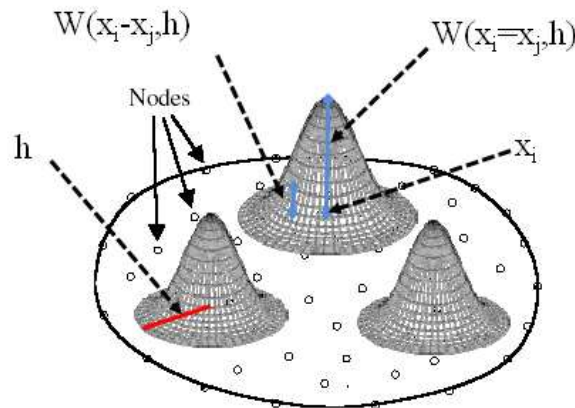

Fig. 1. Meshless Continuum with Weight Functions

The weight, smoothing or kernel function $W(x-x_i)$ scales the contribution of a support node to the field values depending on the distance between the nodes. The choice of the weighting is up to the user. Historically, Gaussian functions were used, though the current consensus favours spline functions like the cubic B-spline [9]:

$$W(x-x',h) = W(u,h) = \frac{1}{h(u)^d}\theta(u)$$

(4)

where d is the number of dimensions and h is the so called smoothing length, which depends on the nodal distances and time.

$$\theta(u) = C \times \begin{cases} 1 - \frac{3}{2}u^2 + \frac{3}{4}u^3 & \text{for u} \le 1 \\ \frac{1}{4}\left(2-u^3\right) & \text{for } 1 \le \text{u} \le 2 \\ 0 & \text{for u} > 2 \end{cases}$$

(5)

where C is a constant of normalization. There are no strict rules, regulating which weight function has to be to chosen. In effect, any function can be used, which fulfils the following properties [13]:

− W(x-x',h) decreases monotonically with increasing x-x'.
− W(x-x',h) is always equal or larger than zero
− W(x-x',h) is compact, i.e. weighting function is zero outside of the support area.
− The integral of W(x-x',h) over support area is unity.

The SPH approximation of the derivative $\nabla f(x)$ of a function $f(x)$ can be derived by replacing $f(x)$ with $\nabla f(x)$ in Eq. 1 [13], leading to the term:

$$\nabla f(x) = -\int_{\Omega} f(x') \cdot \nabla W(x-x',h)dx'$$

$$\text{resp. } \nabla f(x_i) = -\sum_{j=1}^{N} \frac{m_j}{\rho_j} f(x_j) \cdot \nabla W(x-x_j,h)$$

(6)

with the derivative $\nabla W(x-x',h)$:

$$\nabla W(x_i - x_j, h) = \frac{x_i - x_j}{h}\frac{\partial W}{\partial h}$$

(7)

This means that the derivative of a SPH representation is approximated by weighting the support nodes with the derivative of the weight function W(x-x',h).

While the SPH method is robust to large deformation, several problems can be encountered:

1. The SPH approximation leads to field values which in general differ from the nodal values at the same coordinate, i.e. the field values are not interpolated. This poses a problem in the imposition of essential boundary conditions, because it is not possible to directly assign the boundary conditions on the nodes. The available solutions are case dependant and can lead to numerical instabilities or inaccurate

results.

2. Bodies are discretised by nodes, which are placed inside the body, but not directly on the boundaries. The surfaces are therefore not exactly modelled, but rather approximated by the field approximations. In the case of LS-DYNA, the original boundaries are completely disregarded and contact is calculated directly on the SPH-nodes.

3. In contrast to a structured mesh, where the nodes have defined connections to the other nodes, no such connection exists with SPH-nodes. Nodes that have been separated from the rest of the body can reattach as soon as other nodes come within the smoothing range of their weighting functions.

3. EXPERIMENTAL SETUP

For the experimental part a single diamond grain is brazed onto a stainless steel pin. The synthetic diamond grain has the size D851. In Fig. 2b the brazed single diamond grain pin can be seen. The positioning of the brazed steel pin, i.e. the orientation of the diamond, towards the cutting direction is managed using an optical light microscope (cf. Fig. 2a). Afterwards the pin is mounted in the spindle of a conventional CNC milling machine, as shown in Fig. 2c. The single diamond grain pin mounted in the spindle moves across the work piece of 90MnCrV8 steel and scratches into it. The cutting speed was 0.18 m/s. Instead of being fully even the workpiece was slightly tilted, which in turn led to a gradual increase in cutting depth and therefore also in cutting force. During the scratch creation the values of the cutting, the normal and the tangential force were recorded with a Kistler dynamometer MiniDyn 9256C1. By means of the white-light interferometry microscope Zygo NV5000 the scratch topography was determined for obtaining information about scratch profile, cutting area and cutting depth.
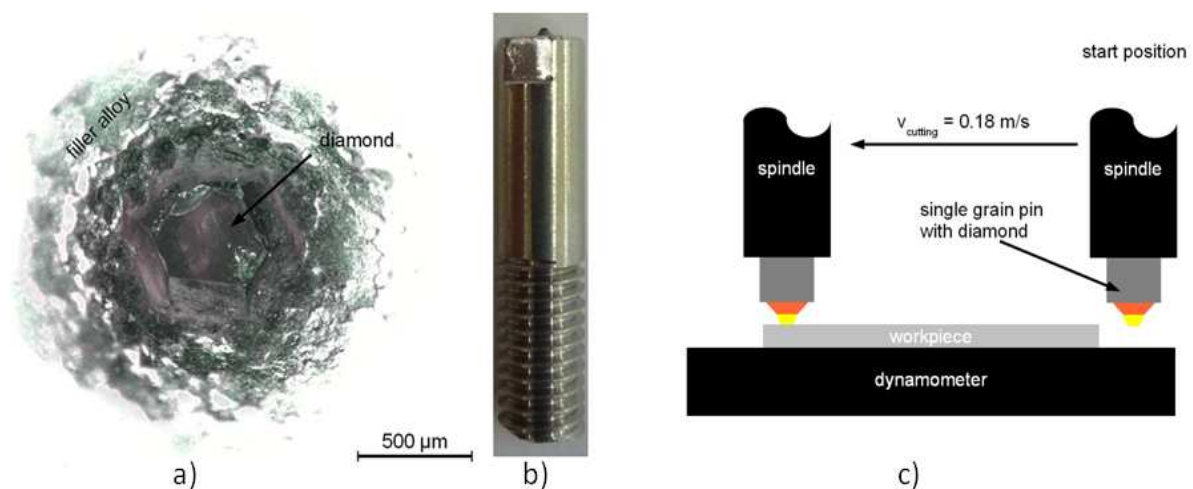

Fig. 2. Test Setup

4. MODELLING OF SINGLE GRAIN CUTTING

The cutting test set-up presented a design challenge in the form of the ratio of the involved length scales. The edges of the diamond are 50 to 100 times longer than the depth of cut, ranging from 0.5 to 10 μm. For a faithful representation of the problem geometry, one has either to generate a huge amount of nodes, to decrease the node density and thereby the accuracy or scale the problem geometry. Due to the linear dependence of the cutting force on the chip width, a scaling of the diamond geometry perpendicular to the cutting direction has been chosen. In this case, the diamond edges are scaled down to an edge length of 50 μm. The validation simulations using cubic grains showed no significant influence on the scaled cutting forces.

The used diamond shapes are shown in Fig. 3. The geometries 3a and 3b show a hexa-octoedric diamond which was also used in the experiments. In case 3a, the diamond is placed on a hexahedral face with a rectangular face as the main cutting face. In case 3b, the grain is placed on the rectangular face. The cube in Fig. 3c is used for multiple grain cutting simulations due to lower computational cost.
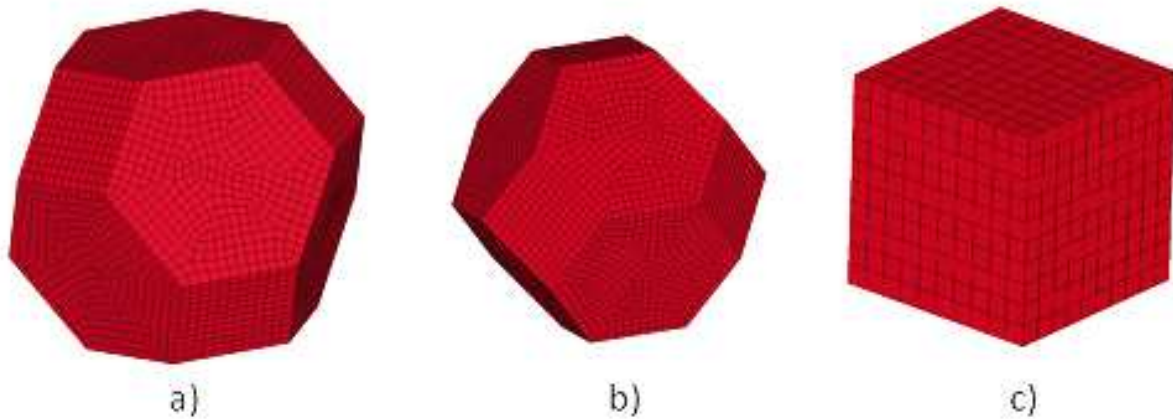

Fig. 3. Cutting Grain Geometry

The work piece is modelled with a length L_{WP} of 0.5 mm, a height H_{WP} of 0.03mm and a width W_{WP} of 0.2 mm. The work piece is discretised with a mesh density of $8 \cdot 10^6$ nodes/mm³ for cubes with zero pitch angle, respectively $64 \cdot 10^6$ nodes/mm³ for surfaces with a rake angle larger than zero. The cutting depth D is chosen as 10 μm. The simulation setup can be seen in Fig. 4.

In order to model the high strains and strain rates in the cutting process a Johnson-Cook Material Model [11] is chosen:

$$\sigma_y = \left(A + B \cdot \overline{\varepsilon}_{pl}^n\right) \cdot \left(1 + C \cdot \ln\left(\frac{\dot{\overline{\varepsilon}}}{\dot{\overline{\varepsilon}}_0}\right)\right)\left(1 - \left[\frac{T - T_{ref}}{T_{melt} - T_{ref}}\right]^m\right) \tag{8}$$

where σ_y is the yield stress, $\bar{\varepsilon}_{pl}$ is the equivalent plastic strain, $\dot{\bar{\varepsilon}}$ and $\dot{\bar{\varepsilon}}_0$ are the actual and reference effective strain rate and T_{ref} and T_{melt} are the reference and the melting temperature of the material, respectively. Due to the low experimental cutting speeds, and therefore low friction heat temperature effects on the yield stress are discarded.
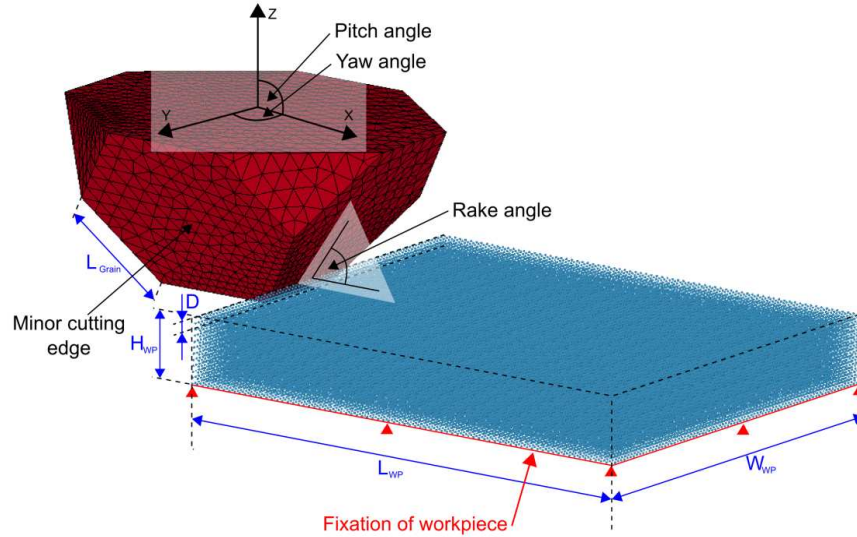

Fig. 4. Simulation Setup

A simple linear equation of state using the bulk modulus is used to model the connection between strain and pressure.

The Johnson Cook model also includes damage, which is used in the simulation of multiple grain cutting. The evolution equation for the damage variable is:

$$\varepsilon_f = \left[D_1 + D_2 \cdot \exp\left(D_3 \frac{p}{\bar{\sigma}} \right) \right] \cdot \left[1 + D_4 \ln \frac{\dot{\bar{\varepsilon}}_p}{\dot{\bar{\varepsilon}}_0} \right] \cdot \left[1 + D_5 \left(\frac{T - T_{ref}}{T_{melt} - T_{ref}} \right) \right] \tag{9}$$

where p is the hydrostatic pressure, $\bar{\sigma}$ the equivalent von Mises stress, and D_1 to D_5 are the damage parameters, which model the influence of the strain, the strain rate and the temperature on the material failure. Rupture occurs if the accumulated ε_f over all time steps reaches unity. In the implemented SPH-Method, nodes reaching the failure limit stop to be used as support nodes, but are still present in the body. It should be noted that a failure model using meshless methods is not necessary to simulate the chip separation in metal cutting as material failure is handled by simply moving the nodes out of the smoothing distance.

As a starting point, the material parameters have been adapted from [25]. These parameters proved unsuitable, as the cutting forces were underestimated by 70%. This discrepancy is supposed to be due to the size effect at small cutting depths, which is difficult to model with common material models. To improve the material model, microhardness tests using a Vickers indenter were performed and the material parameters were fitted to the

test data using simulations of the indentation test. The diamond grain is modelled as rigid body with the material data used for contact calculations. All material data can be seen in Table 1.

Table 1. Material parameters

E_{steel}	[GPa]	275	n	[-]	0.14	D3	[-]	-2.272
ν_{steel}	[-]	0.28	C	[-]	0.01	D4	[-]	0.002
ρ_{steel}	[Kg/ m^3]	7850	$\dot{\varepsilon}_0$	[1/sec]	10e-6	E_{Diam}	[GPa]	1060
A	[GPa]	4	D1	[-]	0.05	ν_{diam}	[-]	0.07
B	[GPa]	0.5	D2	[-]	1.873	ρ_{diam}	Kg/m^3	3500

5. SIMULATION RESULTS

The simulation approach is separated into three steps. The first step consists of the simulation of the real diamond grain geometries as a mean to validate the basic simulation setup and material data. In a second step, the influence of the yaw angle on the cutting forces, the burr generation and the chip removal rate is analysed. In a third step, simple cubic grains are used to simulate the consecutive cutting of multiple grains.

5.1. SIMULATION OF REAL DIAMOND CUTTING GRAINS

Two different grain placements are simulated as shown in Fig. 4a and 4b; in case 1 the diamond grain is placed on a rectangular face, in case 2 it is placed on a hexahedral face. A direct comparison of the resulting simulated and experimental forces is not possible, as the simulated diamonds have been scaled down. Instead, the Kienzle-Victor parameter k_c is used to compare the cutting forces and the ratio between the cutting and the normal force is used to assess the normal force. The Kienzle-Victor parameter is defined as the ratio between cutting force F_c and chip area A_c:

$$k_c = F_c/A_c = F_c/D \cdot b \tag{10}$$

As shown in Fig. 5, the k_c values are underestimated in case 1 by 30%, though the general characteristic of a maximum of k_c at 22.5° has been captured.

This error may be attributed to the material modelling. It does not take the size effect, which is inherent to microcutting processes, into account. The Johnson-Cook Model, while suited to high strain and strain rate problems, has no special mechanism to cope with the size effect, and further additions to the material model may be necessary. The simulated

cutting/normal force ratio predicted the experimental results within a few percent with exception of a yaw angle of 0°.

This may be the result of an inaccurate representation of the so called dead zone which is built up in front of the main cutting face. This dead zone, as reported by [18], is a region in front of the cutting faces with a negative rake angle below a process dependant threshold angle where the work piece material moves with the cutting edge and generates a new cutting geometry in front of the tool. It can be identified from the simulation data. As shown in Fig. 6b, the zone is characterised by high plastic strains.
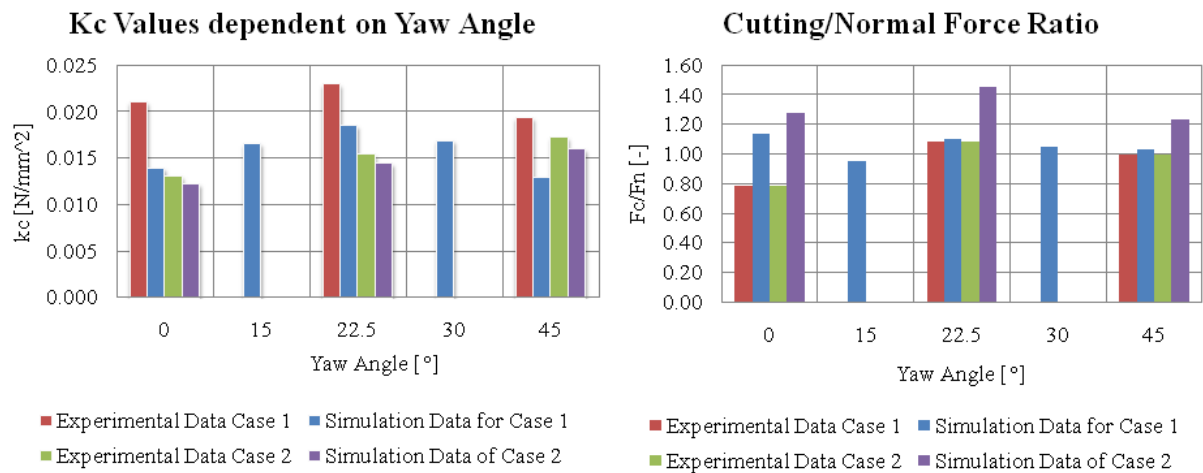

Fig. 5. Simulated and Experimental kc and Cutting/Normal Force Ratio for hexa-octoedric Grain
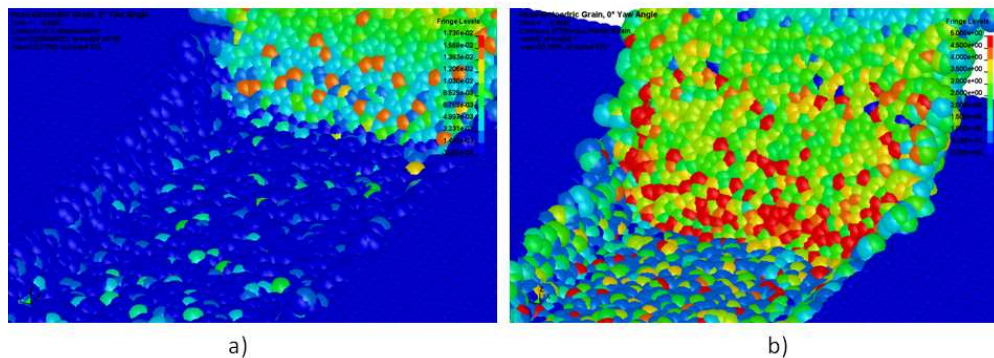

Fig. 6. Dead zone in cutting with negative rake angles

Due to the fact that the regions of high strain can occur elsewhere on the sidewalls of the cutting groove, the plastic strain has ultimately not been used as detection criterion. Instead, the total nodal displacement Fig. 6a has been chosen as a detection criterion. The nodes with a displacement in the cutting direction larger than a critical value of $u_x = 100$ μm and a displacement normal to the cutting direction of $u_y = 10$μm are detected as nodes belonging to a dead zone. The high plastic strains which are reached in the dead zone can cause numerical instabilities due to the extremely high stresses which are induced in the material. This is a deficiency of the material model; in reality, the zone becomes practically

rigid and forms a part of the cutting geometry, with additional material flowing around the tool and the dead zone. Due to the exponential nature of the hardening law, SPH nodes captured in this dead zone continue to harden, reaching plastic strain values above 20. A further study of the material modelling and the influence of the dead zone on the process results would be beneficial.

5.2. BURR GENERATION AND CHIP REMOVAL RATE

Burrs, also referred as side ridges in [1], are formed when displaced material is not removed as a chip or pressed below the cutting grain. In this case the material is deposited on the side of the cutting groove and negatively impacts the surface quality of the work piece. In the simulations, two different mechanisms for burr generation could be observed; First, as shown in Fig. 7a, small burrs are formed on the side faces of the grain, inclined towards the groove. Due to the resulting forces, material from the sidewalls is pressed forwards and upwards and is deposited as a burr. The second mechanism, shown in Fig. 7b, works on the minor cutting faces with small yaw angles relative to the cutting direction. Instead of being cut, the material slides along the grain and is deposited as a burr behind the trailing edges.
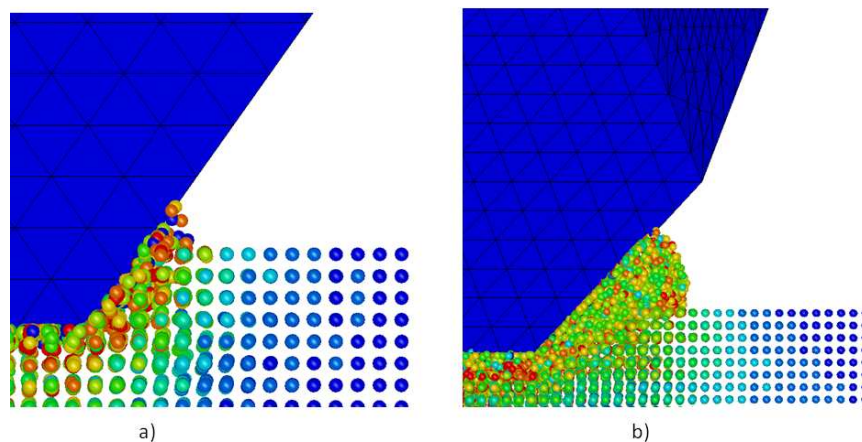

Fig. 7. Burr Generation

Depending on the amount of material in front of the minor cutting face, the amount is several times the mass of the material deposited by the side faces of the grain. The variations of the yaw angle show a chip-burr transition at angles between 35 and 40°, though friction and the length of the minor cutting face influence this behaviour as well. The transition between burr and chip generation is not abrupt. The change is announced by a rising amount of vertical ruptures in the burr. For this given grain geometry, a grain should therefore ideally be placed in a way that avoids yaw angles below 40°. At least, the cutting face with the lowest side length should be placed as burr producing cutting face, in order to

minimize the amount of material deposited as burr.

By following the argumentation of the burr generation, the chip removal rate η can be postulated to be a function of the ratio of the chip producing cutting faces A_{CF} divided by the sum of all cutting faces A_{total} times the cut volume $\dot{V}_c$:

$$\eta_c = A_{CF} \Big/ A_{total} \cdot \dot{V}_c \qquad (11)$$

5.3. MULTIPLE-GRAIN CUTTING

This section presents the research on the interactions of multiple grains, as shown in Fig. 8. Two grains are placed in sequence with an offset perpendicular to the cutting direction from +25 μm to -10 μm overlap between the grains. In case 1, two cubic grains with zero yaw angles are used in sequence. In case 2 the leading grain has a yaw angle of 15°. As shown in the right hand side of Fig. 8, the k_c values for the leading grain remain stable with small deviations due to numerical inaccuracies. The cutting forces for the trailing grain in case 1 remain also practically constant. For the trailing grain in case 2, a definite increase of kc is visible for a larger overlap. This is due to the deposition of a significant burr from the minor cutting face of the leading grain. The additional mass has to be moved and the higher yield stresses due to work hardening locally increase the cutting force. With a higher overlap the active cutting area of the trailing grain becomes lower, shifting the averaged k_c ratio to higher values.
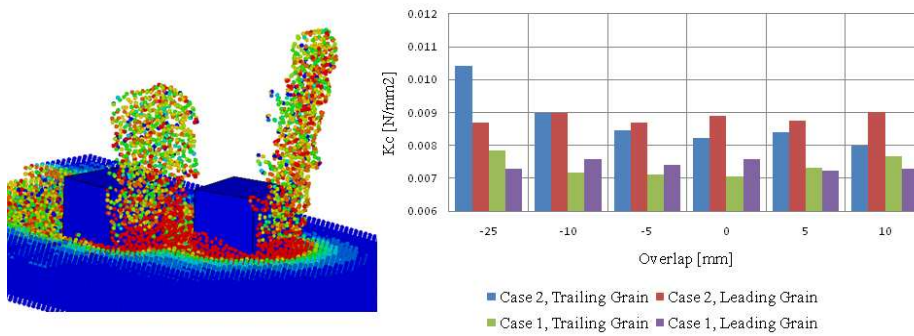

Fig. 8. Multi-grain cutting configuration and forces

6. CONCLUSIONS

The utility of using SPH in modeling single grain cutting simulations has been shown. The consistency of the simulation results with the measured data is acceptable in the view that further work in the area of material modeling is necessary. A dead zone in the case of negative rake angles is reproduced by the simulations as well. Two different mechanisms for the formation of a burr - sidewall displacement and cutting face sliding - have been identified and the dependence of the latter on the yaw angle has been shown. There exists

a lower boundary for the yaw angle of a cutting face in order to avoid an excessive burr generation due to cutting face sliding.

In the simulation of multiple grains, the effect of the work hardened material and of the burr on the cutting behaviour of subsequent grains has been shown. The grains producing burrs not only impede the surface quality, but also increase the force necessary for the subsequent grains to cut their assigned material path.

REFERENCES

[1]   ABEBE M., APPL F., 1988, *Theoretical analysis of the basic mechanics of abrasive processes*, Wear 126, 251-266.
[2]   AURICH J.C., BRAUN O., WARNECKE G., 2003, *Development of a superabrasive grinding wheel with defined grain structure using kinematic simulation*, Cirp Annals-Manufacturing Technology, 52/1, 275-280.
[3]   BRAUN O., WARNECKE G., AURICH J.C., 2005, *Simulation-based development of a superabrasive grinding wheel with defined grain structure*, in *Transactions of the North American Manufacturing Research Institution of SME, 33,* 351-358.
[4]   BRINKSMEIER E., GIWERZEW A., 2003, *Chip formation mechanisms in grinding at low speeds*, Cirp Annals-Manufacturing Technology, 52/1, 253-258.
[5]   BURKHARD G., 2001, *Spanen mit definiert angeordneten Hartstoffkörnern*, VDI Verlag Düsseldorf, 591.
[6]   BURKHARD G., REHSTEINER F., 2002, *High efficiency abrasive tool for honing*, Cirp Annals-Manufacturing Technology, 51/1, 271-274.
[7]   CALAMAZ M., LIMIDO J., NOUARI M., ESPINOSS C., COUPARD D., SALAUN M., GIROTA F., CHIERAGATTI R., 2008, *Toward a better understanding of tool wear effect through a comparison between experiments and SPH numerical modelling of machining hard materials*, International Journal of Refractory Metals and Hard Materials, 27, 3.
[8]   DOMAN D., WARKENTIN A., BAUER R., 2009, *Finite element modeling approaches in grinding*, International Journal of Machine Tools and Manufacture, 49, 109-116.
[9]   HALLQUIST J. O., 2009, *LS-DYNA KEYWORD USER'S MANUAL Volume I'*, LSTC, Version 971, Revision 4.
[10]   HEINSTEIN M., SEGALMAN D., 1997, *Simulation of Orthogonal Cutting with Smooth Particle Hydrodynamics*, SANDIA REPORT SAND97–1961 , Sandia National Laboratories.
[11]   JOHNSON G., COOK W., 1985, *Fracture characteristics of three metals subjected to various strains, strain rates, temperatures and pressures*, Eng. Frac. Mech. 21, 33-48.
[12]   LIMIDO J., ESPINOSA C., SALAUN M., LACOME J., 2006, *A new approach of high speed cutting modelling:SPH method*, J. Phys. IV France 134, 195-200.
[13]   LIU G.R. 2009., *Mesh Free Methods: Moving Beyond the Finite Element Method,* CRC Press.
[14]   LUCY L. B., 1977, *A numerical approach to the testing of the fission hypothesis*, The Astronomical Journal 82, 1019.
[15]   MATSUO T., TOYOURA S., OSHIMA E., OHBUCHI Y., 1989, *Effect of grain shape on cutting force in superabrasive single-grit tests*, CIRP, 38/1, 323-326.
[16]   MONAGHAN J., GINGOLD R., 1977, *Smoothed Particle Hydrodynamics - Theory and application to non-spherical stars*, Royal Astronomical Society 181, 543-574.
[17]   OEZEL T., ZEREN E., 2007, *Numerical modelling of meso-scale finish machining with finite edge radius tools*, I nternational Journal of Machining and Machinability of Materials 2/3-4, 451-468.
[18]   OHBUCHI Y., MATSUO T., 1991, *Force and chip formation on single-grit orthogonal cutting with shaped CBN and diamond grains*, CIRP, 40/1, 327-330.
[19]   OPOZ T. T., CHEN X., 2010, *Numerical Simulation of Single Grit Grinding*, Proc. of the 16th International Conference on Automation, Computing.
[20]   PARK H. W., LIANG S. Y., 2009, *Force modeling of microscale grinding process incorporating thermal effects*, The International Journal of Advanced Manufacturing Technology, 44, 476-486.
[21]   PINTO F.W., VARGAS G.E., WEGENER K., 2008, *Simulation for optimizing grain pattern on Engineered Grinding Tools*, Cirp Annals-Manufacturing Technology, 57/1, 353-356.
[22]   SUNG C.M., 1999, *Brazed diamond grid: a revolutionary design for diamond saws*, Diamond and Related Materials, 8/8-9, 1540-1543.

[23] SUNG J.C., SUNG M., 2009., *The brazing of diamond*, International Journal of Refractory Metals and Hard Materials, 27, 382-393.

[24] VILLUMSEN M. F., FAUERHOLDT T. G., 2008,. *Simulation of Metal Cutting using Smooth Particle Hydrodynamics*, LS-DYNA Anwenderforum.

[25] WEBER M., HOCHRAINER T., GUMBSCH P., AUTENRIETH H., DELONNOY L., SCHULZE V., LOUMLHE D., KOTSCHENREUTHER J., FLEISCHER J., 2007, *Investigation of Size-effects in Machining with Geometrically Defined Cutting Edges*, Machining Science and Technology,11, 447-473.

[26] WEBSTER J., TRICARD M., 2004, *Innovations in abrasive products for precision grinding*, Cirp Annals-Manufacturing Technology, 53/2, 597-617.

[27] WEGENER K., PINTO F.W., KUSTER F., VARGAS G.E., TRANSCHEL R., 2010, *Simulation zur Optimierung von Schleifwerkzeugen mit definierter Kornanordnung*, Diamond Business, 2, 28-33.